Chemistry, Physics and Technology of Surface. 2023. V. 14. N 4. P. 474-494

PACS: 61.43.Gt; 68.35.–p; 68.43.–h doi: 10.15407/hftp14.04.474

V.M. Gun'ko, O.K. Matkovsky

ADSORPTION OF VARIOUS COMPOUNDS ONTO NANOOXIDES UNMODIFIED AND DIFFERENTLY PRETREATED

Chuiko Institute of Surface Chemistry of National Academy of Sciences of Ukraine
17 General Naumov Str., Kyiv, 03164, Ukraine, E-mail: vlad_gunko@ukr.net

Features of interfacial adsorbate/adsorbent phenomena depend on several factors: particulate morphology, texture, and structure of adsorbents, molecular weight, shape, and polarity of adsorbates; as well as prehistory of adsorbents pretreated under different conditions. All these factors could affect the efficiency of practical applications of not only adsorbents but also polymer fillers, carriers, catalysts, etc. Interactions of nonpolar nitrogen, hexane, benzene, weakly polar acetonitrile, and polar diethylamine, triethylamine, and water with individual (silica, alumina), binary (silica/alumina (SA)) and ternary (alumina/silica/titania, AST) nanooxides were studied using experimental and theoretical methods to elucidate the influence of the morphological and textural characteristics and surface composition of the materials on the adsorption phenomena. The specific surface area S_X/S_{N_2} ratio (X is an adsorbate) changes from 0.7 for hexane adsorbed onto amorphous silica/alumina SA8 with 8 wt. % Al_2O_3 (degassed at 200 °C) to 1.9 for acetonitrile adsorbed onto pure fumed alumina (treated at 900 °C). These changes are relatively large because of variations in orientation, lateral interactions, and adsorption compressing of organic molecules interacting with surfaces characterized by certain set and amounts of various active sites, as well as due to changes in the accessibility of pore surface for probe molecules of different sizes. Larger $S_X/S_{N_2} > 1$ values are observed for complex fumed oxides with larger primary nanoparticles, greater surface roughness, hydrophilicity, and Brønsted and Lewis acidity of a surface. Both polar and nonpolar adsorbates can change the morphology and texture of aggregates of oxide nanoparticles, e.g., swelling of structures, compacted during various pretreatments, upon the adsorption of liquids. The studied effects should be considered upon practical applications of adsorbents, especially "soft" fumed oxides.

Keywords: *oxide nanoparticles, complex nanooxides, textural characteristics, nonpolar adsorbates, polar adsorbates, interfacial phenomena*

INTRODUCTION

Fumed metal or metalloid oxides (FMO) composed of nanosized primary particles (therefore, these materials are named as 'nanooxides') such as silica, alumina, titania, and some others are widely used in industry, biotechnology, and medicine as adsorbents, polymer fillers, drug carries, additives, pigments, catalysts, *etc.* [1–15]. The physicochemical properties and characteristics of FMO can be varied during the synthesis using small amounts of dopants (typically forming solid solution in a host matrix) or a blend of different precursors of comparable amounts that form separated or/and interpenetrated phases that can be amorphous or/and crystalline [4–9, 15–23]. The flame conditions: temperature, its gradient, ignition torch length, flow turbulence and speed, as well as the O_2/H_2 ratio and precursor amounts can strongly affect all FMO characteristics [4–9]. The surface and volume contents, phase composition and crystallinity of different oxides in complex nanoparticles could be varied in complex FMO (due to controlled changes in the synthesis conditions) [16–22] as well as their specific surface area (SSA, S_{BET}), surface roughness, and particle aggregation responsible for textural porosity of the powders and other important characteristics of the materials being in different media [24–34]. The SSA value is determined by primary nonporous nanoparticle (NPNP) size distribution (NPSD) because $d_{av} \approx c/(\rho_0 S_{BET})$, where d_{av} is the average diameter (or the first moment of NPSD) of NPNP, c is a constant, and ρ_0 is the true density of the material [35, 36]. Typically, the NPSD dispersion increases with increasing d_{av} value [4, 35, 36]. Changes in the structural, textural, and morphological characteristics of FMO affect the interactions of

nanoparticles with their surroundings (*e.g.*, with adsorbates, liquids, filled polymers, *etc.*) [35–39], the adsorption properties with respect to polar and nonpolar adsorbates, and other characteristics important for the practical applications of the materials [1–15, 40–50]. An additional way to change practically important FMO characteristics is NPNP surface modification by organic or organometallic compounds [4, 16, 17, 24–28]. The first stage of the modification is the adsorption of modifiers onto oxide nanoparticles, and features of the interfacial phenomena could determine the degree of the surface modification. As a whole, the adsorption phenomena play an important role in many applications of FMO. Detailed analysis of the effects of the NPSD, SSA value, aggregation, and composition of nanoparticles on the adsorption of both polar and nonpolar adsorbates can be useful to provide a deeper insight into the interfacial phenomena and the behavior of FMO in different and practically important systems. It is known [35, 36, 51–61] that the effective SSA (*i.e.*, surface area accessible for given adsorbate molecules) of FMO decreases with increasing molecular size of the adsorbates, despite the fact that the primary nanoparticles are nonporous. This effect is due to aggregation of NPNP (formation of supra–NPNP structures) [30–35], and narrower voids between NPNP in aggregates could be inaccessible for larger probe molecules [36]. There is an additional aspect related to toxic properties of the nanomaterials that depend on the surface composition (*e.g.*, FMO surface modification could reduce these properties), NPSD, features of NPNP interactions with surroundings, *etc.* [62–66]. However, systematic comparative experimental and theoretical investigations of the adsorption of different nonpolar, weakly polar, and polar adsorbates onto composite FMO are rather incomplete [15–17, 35, 36, 67–74] because a set of adsorbates and adsorbents could be increased, theoretical models should be improved as well as the analysis of the textural characteristics of FMO, especially complex ones. Therefore, the aim of this work was to study the adsorption of a large set of adsorbates: nonpolar nitrogen, benzene, and hexane, weakly polar acetonitrile, and polar diethylamine, triethylamine, and water (functional groups of these probes can be representatives for many other compounds) onto individual and complex FMO (using representative samples) using experimental methods and quantum chemical calculations with improved cluster models.

MATERIALS

Individual fumed silica (a set of A–300 samples synthesized under different flame conditions with SSA from 260 to 319 m^2/g), alumina (two samples) and mixed oxides SiO_2/Al_2O_3 (SA8 and SA23 at alumina content $C_{Al_2O_3}$ = 8 and 23 wt. %, respectively), and $Al_2O_3/SiO_2/TiO_2$ (AST03 and AST1) with alumina as a main component (FMO composition and treatment conditions are shown in Tables 1–3) (Pilot plant of the Chuiko Institute of Surface Chemistry, Kalush, Ukraine) were heated at 200 °C for several hours to remove adsorbed compounds and residual HCl and additionally degassed for 2 h before adsorption measurements. Alumina was also preheated at 600 and 900 °C before the probe adsorption. A set of FMO samples (20 wt. % in aqueous suspensions) were cryogelled (Table 2) at –65 °C or –13 °C in cylindrical stainless-steel thick-walled (~ 2 cm) cryo-reactors with thick threading caps providing pressure up to 1000 atm upon complete freezing of water or FMO gelation (20 wt. % in aqueous media) in open vessels at 20 °C and 1 atm [36]. A blend of A–300/AST1 (1:1 w/w) was also studied after different pretreatments. A set of nanosilica samples were synthesized under different conditions affecting the amounts of surface silanols, *i.e.*, the hydrophilicity was varied (Table 3) [16, 35, 36]. Chemical composition of FMO was analyzed using a XRF (Canberra, USA) spectrophotometer with a ^{55}Fe (or ^{109}Cd) radioactive source, and an amplitude analyzer (Canberra) coupled with a computer with the AXIL program. The synthesis, characteristics, and physicochemical properties of individual and complex FMO were described in detail previously [35, 36, 67–74].

ADSORPTION

To analyze the textural characteristics of FMO, low–temperature (–195.8 °C) nitrogen adsorption–desorption isotherms were recorded using a Micromeritics ASAP 2405N adsorption analyzer.

The specific surface area (S_{N_2}) was calculated according to the standard BET method [51, 75]. The total pore volume V_p was evaluated from the nitrogen adsorption at p/p_0 = 0.98–0.99

Table 1. Structural and textural characteristics of the FMO powders degassed at 200 °C

Sample	C_{SiO_2} (wt.%)	C_{TiO_2} (wt.%)	$C_{Al_2O_3}$ (wt.%)	$C^s_{SiO_2}$ (wt.%)	$C^s_{Al_2O_3}$ (wt.%)	d_{av} (nm)	S_{N_2} (m^2/g)	V_{p,N_2} (m^2/g)	S_{ac} (m^2/g)	S_{hex} (m^2/g)	S_{DEA} (m^2/g)	S_{TEA} (m^2/g)
A–300	>99.8	–	0	>99.8	–	9.2	295	0.52		261		
SA8	92	–	8	29.5	70.5	8.6	303	0.68	223	207	271	265
SA23	77	–	23	73.6	26.4	6.9	347	0.82	362	247	434	384
AST1	10.0	1.0	89.0			18.0	99	0.25	180	99	113	117
AST03	2.7	0.3	97.0			13.9	125	0.31	162	101	114	126
Al_2O_3	–	–	>99.8	–	>99.8	19.3	89	0.13	95	90		
Al_2O_3[a]	–	–	>99.8	–	>99.8	12.9	133	0.45	246	187	205	238

Note. C_X (X = SiO_2, TiO_2, and Al_2O_3) denotes the total content of these phases in FMO, and C^s is the surface content of oxides; [a]alumina preheated at 900 °C; d_{av} is the average diameter of FMO nanoparticles estimated from the S_{BET} values; S_X (X = N_2, acetonitrile (ac), *n*-hexane (hex), DEA, and TEA) is the SSA values estimated for monolayer adsorption; $V_{p,N2}$ is the pore volume from the nitrogen adsorption

Table 2. Textural characteristics of unmodified and differently pretreated and degassed FMO estimated from nitrogen adsorption data

Oxide	Medium	T_t (°C)	P_t (atm)	Note	S_{BET} (m^2/g)	S_{nano} (m^2/g)	S_{meso} (m^2/g)	S_{macro} (m^2/g)	V_p (cm^3/g)	V_{nano} (cm^3/g)	V_{meso} (cm^3/g)	V_{macro} (cm^3/g)
A–300	–	–	–	Initial powder	302	94	200	9	0.734	0.035	0.523	0.176
cA–300	water	–65	1000	Cryogel	297	38	258	2	0.827	0.012	0.798	0.017
Al_2O_3	–	–	–	Initial powder	89	12	75	2	0.167	0.006	0.132	0.029
gAl_2O_3	water	20	1	Gel	76	13	60	2	0.545	0.007	0.504	0.034
gsAl_2O	0.1M NaCl	20	1	Gel/NaCl	72	4	43	26	0.521	0.002	0.150	0.369
csAl_2O	0.1M NaCl	–65	1000	Cryogel/NaCl	72	7	44	22	0.553	0.004	0.238	0.311
AST1	–	–	–	Initial powder	83	12	68	3	0.217	0.005	0.166	0.047
gAST1	water	20	1	Gel	74	6	46	22	0.532	0.003	0.231	0.298
cAST1	water	–65	1000	Cryogel	160	15	136	9	0.595	0.008	0.466	0.121
AST03		–	–	Initial								
SA8		–	–	Initial								
SA23		–	–	Initial	347	93	238	15	0.815	0.024	0.526	0.265

Note. Gelation of all other samples (20 wt. % in aqueous media with pure bidistilled water or 0.1 M NaCl solution) was during 12 h at temperature (T_t) –65 °C (cryogel) or 20 °C (gel). Labels in dried samples correspond to cryogel (c), cryogel with NaCl (cs), gelation at room temperature without (gel, g) or with NaCl (gs). Contributions of nanopores (V_{nano} and S_{nano} at pore radius $R < 1$ nm), mesopores (V_{meso} and S_{meso} at 1 nm ≤ R ≤ 25 nm), and macropores (V_{macro} and S_{macro} at $R > 25$ nm) to the total pore volume and SSA are shown

(p and p_0 denote the equilibrium and saturation pressure of nitrogen at –195.8 °C, respectively) [51, 52]. The nitrogen desorption data were used to compute the pore size distributions (PSD, differential $f_V(R) \sim dV_p/dR$ and $f_S(R) \sim dS/dR$) using a self–consistent regularization procedure under non–negativity condition ($f_V(R) \geq 0$ at any pore radius R) at a fixed regularization parameter $\alpha = 0.01$ and a complex pore model with voids between spherical NPNP packed in random aggregates and cylindrical pores (CV/SCR method) [76] developed on the base of methods described elsewhere [35, 36, 77–79]. The differential distribution functions $f_V(R)$ were converted to incremental PSD (IPSD). The errors in the PSD functions include, at least, three sources related to the errors (i) in the adsorption isotherms (< ±1 %); (ii) used pore models (< ± 5 %); and (iii) calculation method. The first one is small because the nitrogen adsorption-desorption isotherms were recorded using top-level equipment. The second and third factors were taking into account using improved CV model of pores with self-consistent regularization procedure. The $f_V(R)$ and $f_S(R)$ functions were also used to calculate contributions of nanopores (V_{nano} and S_{nano} at $R < 1$ nm), mesopores (V_{meso} and S_{meso} at 1 nm ≤ R ≤ 25 nm), and macropores (V_{macro} and S_{macro} at $R > 25$ nm) to the total pore volume and SSA.

Table 3. A set of nanosilica A–300 samples with different hydrophilicity and SSA (S)

Sample number	S (m^2/g)	C_{OH} (μmol/m^2)	$C_{w,105}$ (wt.%)	$C_{w,900}$ (wt.%)	$a_{w,mono}$ (μmol/m^2)
S1	319	3.30	0.5	0.6	3.0
S2	308	3.30	1.3	1.5	4.4
S3	300	3.32	1.8	1.7	8.3
S4	299	3.32	1.8	2.0	8.2
S5	290	3.48	1.0	0.8	9.0
S6	267	3.67	1.6	1.4	8.2
S7	260	3.81	0.6	0.3	4.9

Note. C_{OH} is the surface amount of silanols; $C_{w,105}$ and $C_{w,900}$ are the amounts of water desorbed upon heating at 20–105 °C and 105–900 °C, respectively; and $a_{w,mono}$ is the monolayer capacity for adsorbed water (estimated with Langmuir equation)

To analyze the adsorption characteristics of FMO with respect to various probes, the adsorption of nonpolar *n*-hexane ('hex' was used as a subscript) and benzene, weakly polar acetonitrile (ac), and polar diethylamine (DEA), triethylamine (TEA), and water (w) was studied using an adsorption apparatus with a McBain–Bakr spring quartz scales at ~20 °C [74]. FMO samples were degassed at 10^{-3} Torr and 200 °C for several hours to a constant weight, and then they were cooled to 20±0.2 °C. The measurement accuracy was 1 ± 10^{-3} mg with a relative mean error of ±5%. The surface areas occupied by molecules of acetonitrile ($\sigma = 0.438$ nm^2), hexane (0.744 nm^2), DEA (0.724 nm^2), and TEA (0.760 nm^2) were estimated using quantum chemical calculations. These σ values were used to calculate the specific surface area accessible for various probes (Table 1, S_X). Variations in the S_X values, compared to the $S_{BET,N2}$ values, are due to changes in molecular conformation and surface orientation of the probe adsorbates.

A color indicator *p*-(dimethyl-amino)azobenzene (DMAAB, pK_a = 3.3) was chosen to study active surface sites of representative FMO with optical spectroscopy. The diffuse reflection spectra of adsorbed DMAAB were recorded using a SF–18 (LOMO, St.–Petersburg) spectrophotometer, and then converted to the absorption spectra. The DMAAB adsorption from the gas phase onto FMO samples previously evacuated to 10^{-4} Torr, then heated in special optical glass vessels at defined temperatures for 1 h and hermetically sealed, was carried out at 65±5 °C for 2–4 h. The doses by weight of the FMO samples were chosen to provide similar values of surface area of them. The assignment of the DMAAB absorption bands was carried out with respect to its spectra in neutral and acidic solutions. Four DMAAB bands could be found at (a) $\lambda \approx$ 430–470 nm

(physisorbed DMAAB due to dispersion interaction); (b) 470–490 nm (hydrogen–bonded DMAAB); (c) 490–545 nm (complexes with H^+ transferring from the Brønsted (bridging hydroxyls, B–acid sites) active sites to DMAAB); and (d) 550–560 nm (DMAAB complexes with the Lewis acid sites (L–acid sites) such as incompletely (< 6) O–coordinated Al atoms appeared due to degassing of FMO at relatively high temperature) [35, 36].

HIGH RESOLUTION TRANSMISSION ELECTRON MICROSCOPY (HRTEM)

HRTEM (JEM–2100F, Japan) images were recorded for A–300 (initial and after cryogelation), AST1 (initial and after cryogelation), initial alumina and SA23 as representative FMO samples. A powder sample was added to acetone (for chromatography) and sonicated. Then a drop of the suspension was deposited onto a copper grid with a thin carbon film. After acetone evaporation, sample particles remained on the film were studied with HRTEM.

QUANTUM CHEMICAL CALCULATIONS

Solid nanoparticles (modelled by clusters with 44 polyhedra) with adsorbates (two molecules bound to different active sites) were calculated using electronic density functional theory (DFT) methods with the Gaussian 16 [80] and GAMESS 2022 R2 [81] program suits. The DFT calculations were done using a hybrid functional ωB97X–D and the cc–pVDZ basis set. Some calculations were carried out using *ab initio* method with the cc–pVDZ or 6–31G(d,p) basis sets. The solvation effects were analyzed using the SMD method [82] implemented in the Gaussian and GAMESS. The calculations were performed taking into account zero–point and thermal corrections to the Gibbs free energy in the gas phase and for solvated molecules and silica clusters using the geometry optimized using ωB97X–D/cc–pVDZ (with or without SMD). Some aspects of the interfacial phenomena including adsorption could be elucidated using quantum chemical calculations, especially with consideration of solvation effects onto adsorbates and adsorbent surface. There are several procedures, which can be used to analyze the interaction of adsorbate molecules with a surface of adsorbents, *e.g.*, fragment method with counterpoise corrections (FMCC), Kitaura–Morokuma method, energy decomposition analysis (EDA) with consideration of the basis set superposition errors (BSSE), *etc.* [83–85]. Here three mentioned above methods are used to estimate the interaction energies (Tables 4–6). The distribution functions of atomic charges (CDF) were calculated using a simple equation [86]

$$f_n(q) = (2\pi\sigma_n^2)^{-0.5} \sum_j \frac{\exp[-(q_{n,j} - q)^2]}{2\sigma_n^2}, \qquad (1)$$

where j is the number of an atom of the n-th kind, σ_n^2 is the distribution dispersion for the atoms of the n-th kind, and $q_{n,j}$ is the Mulliken charge value, and q is the current value. The preparation of initial structures, then optimized with the DFT or *ab initio* methods, and final (optimized) structure visualization were performed using the UCSF ChimeraX [87], Avogadro2 [88], Chemcraft [89], and Jmol [90] programs.

RESULTS AND DISCUSSION

Particulate morphology and texture of various FMO. There are several factors strongly affecting the behavior of nonpolar and polar adsorbates bound to a surface of FMO: (i) the particulate and textural characteristics such as NPSD, PSD, SSA, V_p, aggregation of nanoparticles in supra–NPNP structures; (ii) the amounts and distribution of various adsorption sites including surface hydroxyls; (iii) sample history including conditions of the synthesis, preheating, degassing, and subsequent relaxation of strained bonds in surface layers; (iv) molecular sizes and shapes, polarity and polarizability of adsorbates, changes in their conformation upon adsorption; (v) the amounts of adsorbates and the presence of co–adsorbates; and (vi) reconstruction of aggregates of NPNP (< 1 μm), agglomerates of aggregates (> 1 μm), and visible particles (hierarchical three–level supra–NPNP structures) under action of adsorbates.

FMO under such different external actions as heating, suspending, drying, pressing, mechanochemical activation (MCA), even cryogelation at ~ 1000 atm (Fig. 1) typically remain NPNP integrity [35, 36]. However, in the case of the presence of relatively large primary particles of 100–200 nm in sizes (*e.g.*, AST1), these particles could be destroyed under cryogelation at 1000 atm (Fig. 1 *e*, *f*). This effect results in significant increase in the SSA value

(Table 2). For A–300 composed of only small NPNP (5–15 nm), the cryogelation does not lead to decomposition of NPNP (Fig. 1 *a*, *b*), and the SSA value slightly decreases due to compaction of supra–NPNP structures (Table 2). Additionally, for the A–300/AST1 (1:1 w/w) blend, the cryogelation does not lead to decomposition of large AST1 particles because small NPNP of A–300 play a role of a damper [36, 91].

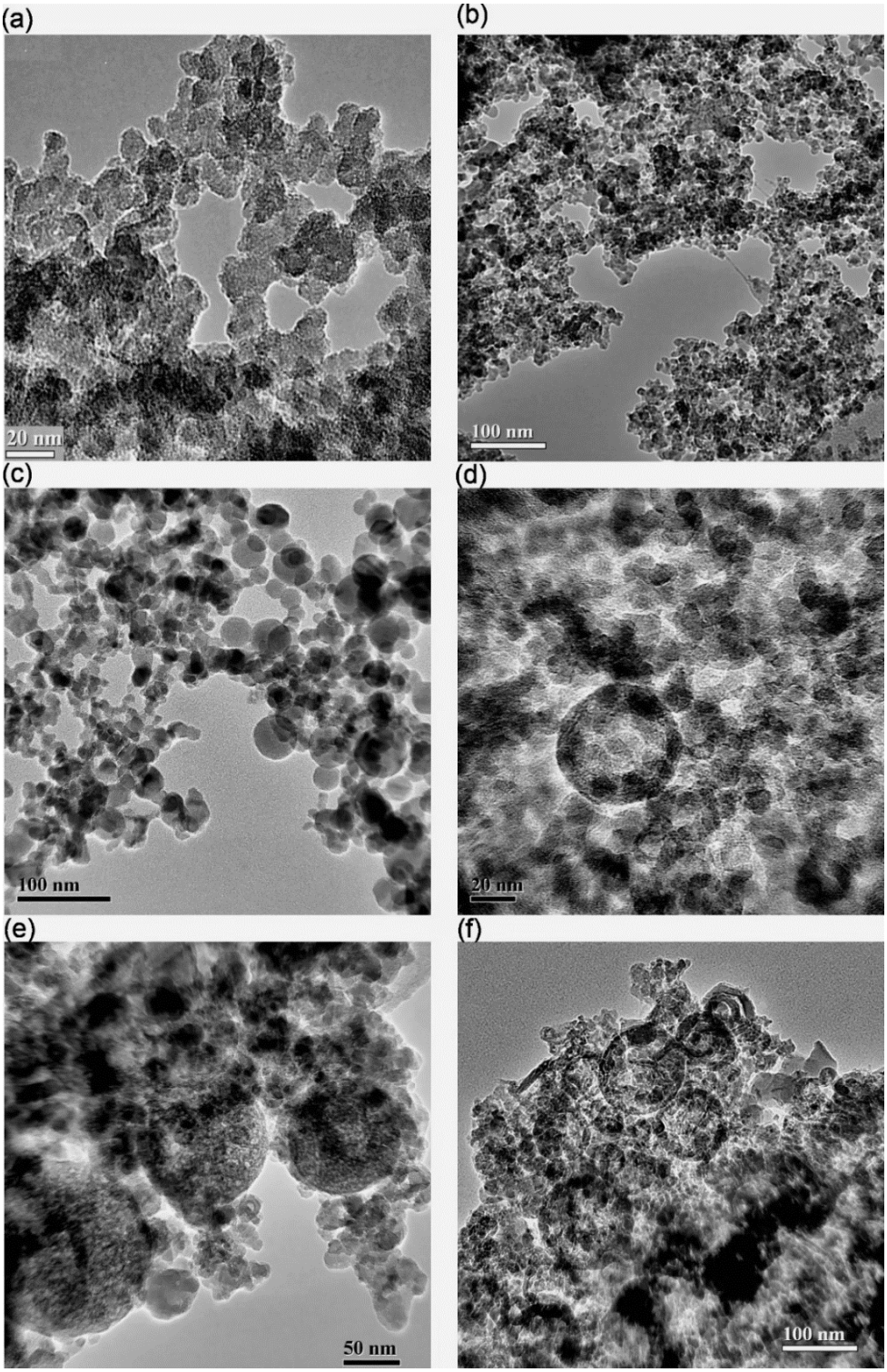

Fig. 1. TEM images of FMO: A–300 (*a*) initial and (*b*) after cryogelation, initial (*c*) alumina, (*d*) SA23, and (*e*) AST1, and (*f*) AST1 after cryogelation (–65 °C, 1000 atm) with destroyed large particles

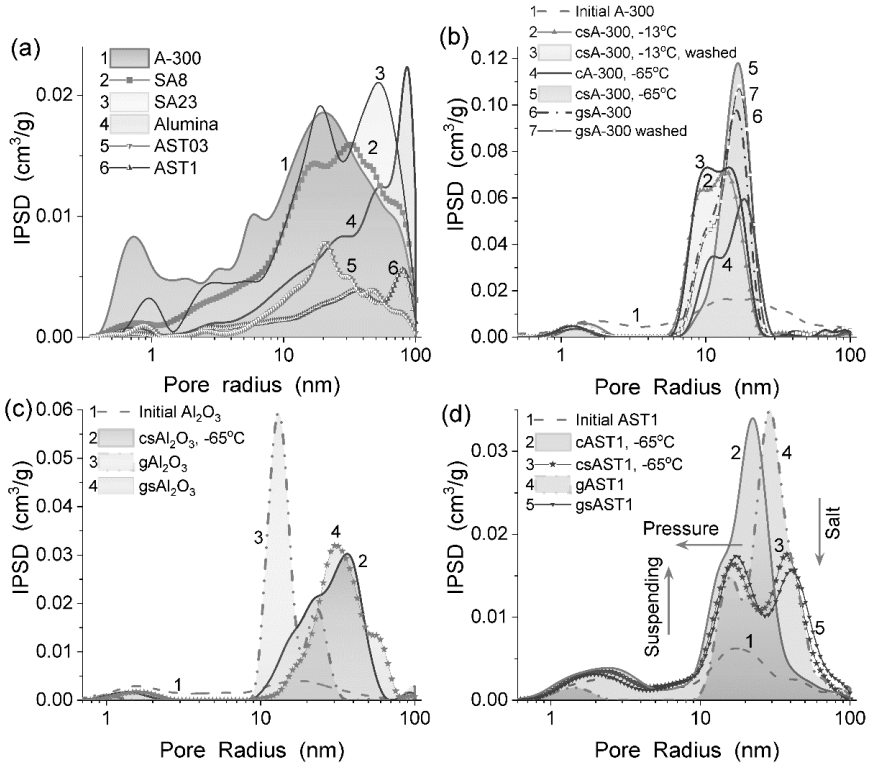

Fig. 2. IPSD (CV/SCR method) of selected FMO initial and differently pretreated: (*a*) initial nanooxides; and pretreated FMO (*b*) A–300, (*c*) alumina, and (*d*) AST1 (cryogelation at –65 or –13 °C and pressure ~ 1000 atm, g – gelation at 20 °C and 1 atm, pure or with 0.1 M NaCl (s), dried and washed at room temperature, see Table 2

Thus, FMO NPNP (< 50 nm in size) are stable under various treatments (with exception of AST1 NPNP > 50 nm in size under high–pressure of cryogelation) in contrast to supra–NPNP structures [35, 36, 70–74]. The supra–NPNP structures are typically compacted under various treatments. The compaction effects depend strongly on conditions, *e.g.*, the amounts of water upon hydro–compaction, gelation, and cryogelation [35, 36, 70–74, 91]. Therefore, pre–history of FMO should be considered upon adsorption measurements because the supra–NPNP compaction results, at least, in certain (sometimes very significant) changes in the textural characteristics of the treated powders.

The FMO PSD (Fig. 2) depend on the NPSD and pretreatment history of samples. Typically, the smaller the NPNP, the stronger their aggregation in the initial powder that results in an increase in contribution of nanopores and narrow mesopores (Fig. 2, Tables 1 and 2) that can differently affect the adsorption of various adsorbates depending on their molecular size and shape. Pretreatment with water (suspending–gelation–drying, cryogelation–drying) results in an increase in contribution of mesopores and macropores due to compaction of supra–NPNP structures. Note that the compaction effects of organic solvents onto the FMO powders are much smaller than that of water [35, 36, 70–74]. However, even upon the adsorption of organics, the hysteresis loops could be open due to rearrangement of supra–NPNP structures (vide infra).

Adsorption results vs. structures of adsorbents and adsorbates. There is an additional effect of aqueous suspending of FMO caused by the difference in their surface composition affecting surface acidity (Fig. 3) and interaction of NPNP in the aqueous suspension due to appearance of surface charges generating repulsive interactions of the particles. Therefore, silica as less acidic than SA (Fig. 3) could be aggregated more strongly upon suspending–drying than complex FMO.

Certain variations in conditions upon the fumed synthesis at high temperatures using metal chlorides or other precursors burned in the $O_2/H_2/N_2$ flame can result in changes in the amounts of surface hydroxyls, *e.g.*, at a silica

surface (Table 3). Their variations for a set of nanosilica A–300 samples, characterized by similar SSA values (Table 3), lead to certain changes in the water adsorption (Fig. 4). As a whole, water better adsorbs onto nanosilicas more hydrophilic with a greater content of silanols (Table 3, Fig. 4) because surface silanols are the main adsorption sites for polar adsorbates bound to nanosilica surface [14–17, 24].

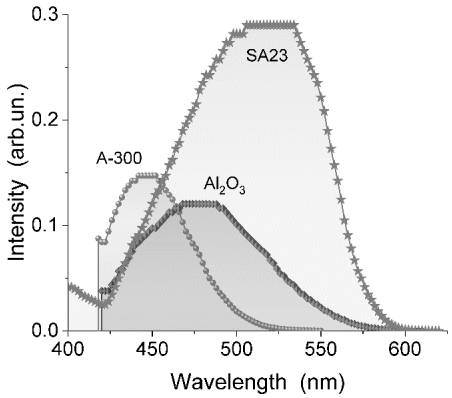

Fig. 3. Optical spectra of DMAAB adsorbed onto fumed silica, alumina, and alumina/silica SA23 (as representative samples)

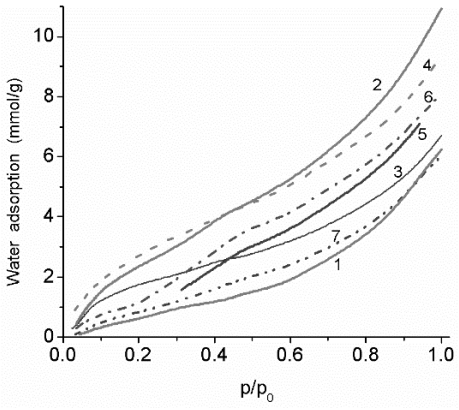

Fig. 4. Water adsorption onto A–300 samples (numbers are in Table 3) characterized by different content of silanols

For all studied FMO, the nitrogen adsorption–desorption isotherms are characterized by narrow hysteresis loops (Figs. 5 and 6), which can be assigned to the type II of the IUPAC classification [51–57]. This regularity is due to a spherical (but non–ideal) shape of nonporous primary particles (Fig. 1) forming hierarchical supra–NPNP structures. Voids between NPNP in supra–NPNP structures provide the textural porosity of the powdered materials with small contribution from nanopores (Fig. 2, Tables 1 and 2) due to the particulate morphology of any FMO. Note that the adsorption isotherms of other studied adsorbates (Figs. 4–8) can be assigned to the type II because of the texture type [51–57] of FMO. The empty volume in loose FMO powders is very great $V_{em} = 1/\rho_b - 1/\rho_0 = 10–25$ cm^3/g (where $\rho_b = 0.04–0.13$ g/cm^3 is the bulk density of the powders). However, after suspending, gelation, or cryogelation and drying–degassing, the textural characteristics strongly change due to supra–NPNP compaction (or even breakage of large AST1 particles, Fig. 1 *e*, *f*) resulting in the formation of the structures similar to xerogels with predominant contribution of meso/macro-pores (Figs. 2 and 4–8, Tables 1 and 2). These textural changes affect the adsorption of any adsorbates onto treated FMO. Fumed oxides with 'soft' supra–NPNP structures are also sensitive to simple aging leading to compaction of the powders and certain mass–transfer from smaller NPNP to larger ones (especially for silica as a hard–flowing liquid) during very long storage; however, crystalline fumed oxides are more stable with respect to the mass–transfer, but the powder compaction during aging is also observed for them [36, 91].

A major contribution of broad macrovoids in supra–NPNP structures (Fig. 2) and thermo-dynamically unfavorable condensation of gases or vapors in such large pores result in ineffectively filling of macrovoids by any gaseous or vapor adsorbates even at $p/p_0 = 0.98–0.99$. For example, the maximal V_{p,N_2} value among studied initial FMO is 0.82 cm^3/g for SA23 ($\rho_b = 0.036$ g/cm^3) (Table 1) (possessing the maximal S_{N_2} value) which corresponds to only ~ 3 % V_{em}. Another effect appearing due to the textural porosity of FMO is that the nitrogen adsorption is proportional to the S_{N_2} value at p/p_0 up to 0.5–0.6 [35, 36] because of weak capillary condensation and insignificant volume filling of broad voids in the FMO powders. Incomplete infilling of macropores is characterized for any gaseous or vapor adsorbates of low–molecular weight bound to FMO (Figs. 4–8). Their adsorption at room temperature is frequently lower than that of nitrogen adsorbed at –195.8 °C.

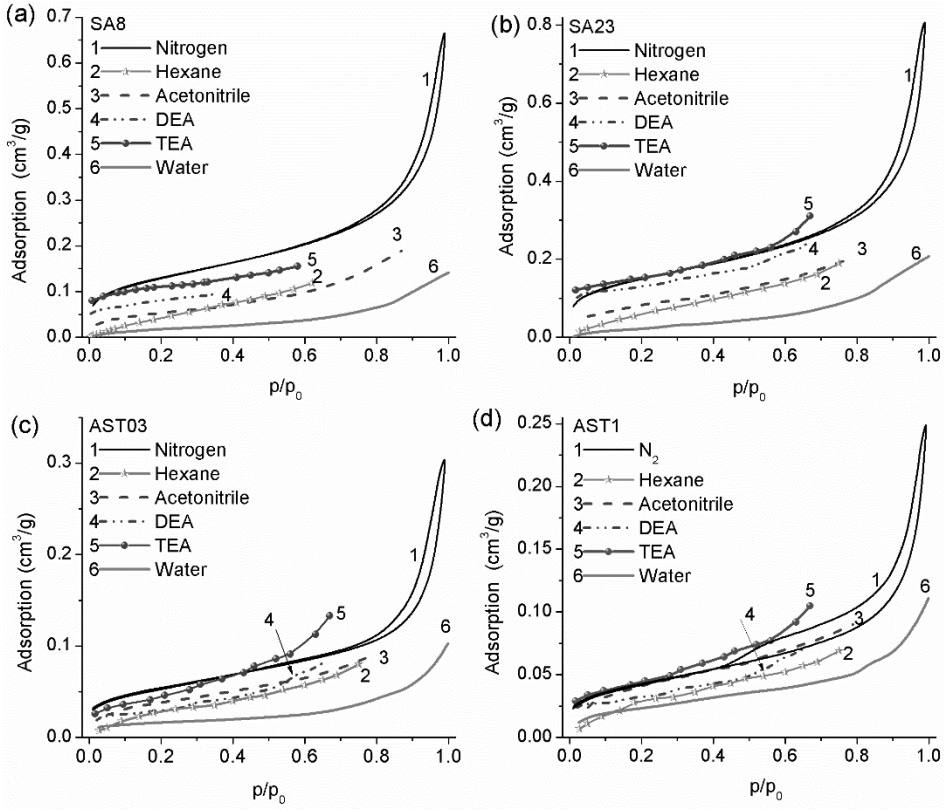

Fig. 5. Comparison of adsorption of different adsorbates (*1*) nitrogen, (*2*) hexane, (*3*) acetonitrile, (*4*) DEA, (*5*) TEA, and (*6*) water onto (*a*) SA8, (*b*) SA23, (*c*) AST03, and (*d*) AST1 degassed at 200 °C

Despite a certain difference in the normalized (divided by S_{N_2}) nitrogen adsorption at $p/p_0 > 0.5$ (Fig. 7 *b*) caused by variations in the NPSD and packing of primary nanoparticles in supra–NPNP, the particulate morphology can be assumed as similar for all FMO studied. This is due to the flame synthesis of FMO at high temperatures $T > 1000$ °C when the primary particles can be in state close to liquid one in the flame that results in the formation of spherical–like NPNP for any FMO. However, the studied FMO powders strongly differ in the SSA, NPSD, PSD, and the aggregation degree of nanoparticles (affecting V_p) that, as well as the difference in the nature of oxide surfaces, can affect the adsorption of any adsorbates (Figs. 1–8, Tables 1–3).

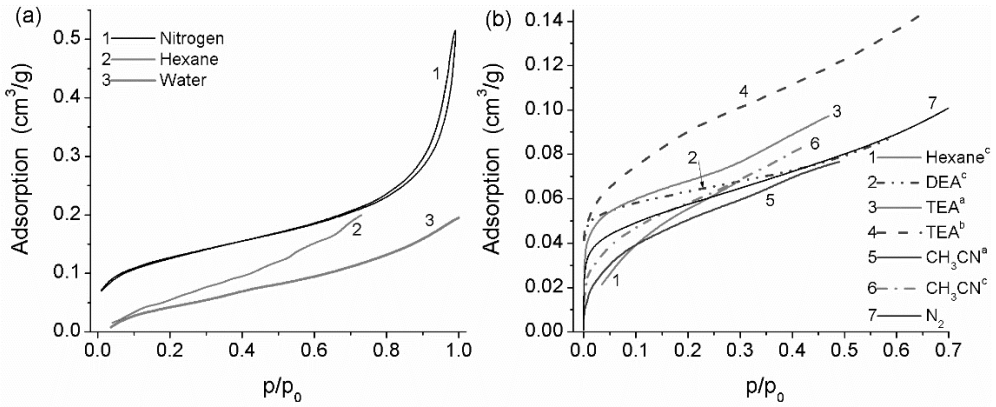

Fig. 6. Adsorption of different adsorbates onto (*a*) A–300 degassed at 200 °C; (*b*) fumed alumina (S_{N_2} = 133 m^2/g) degassed at [a]200, [b]600, and [c]900 °C

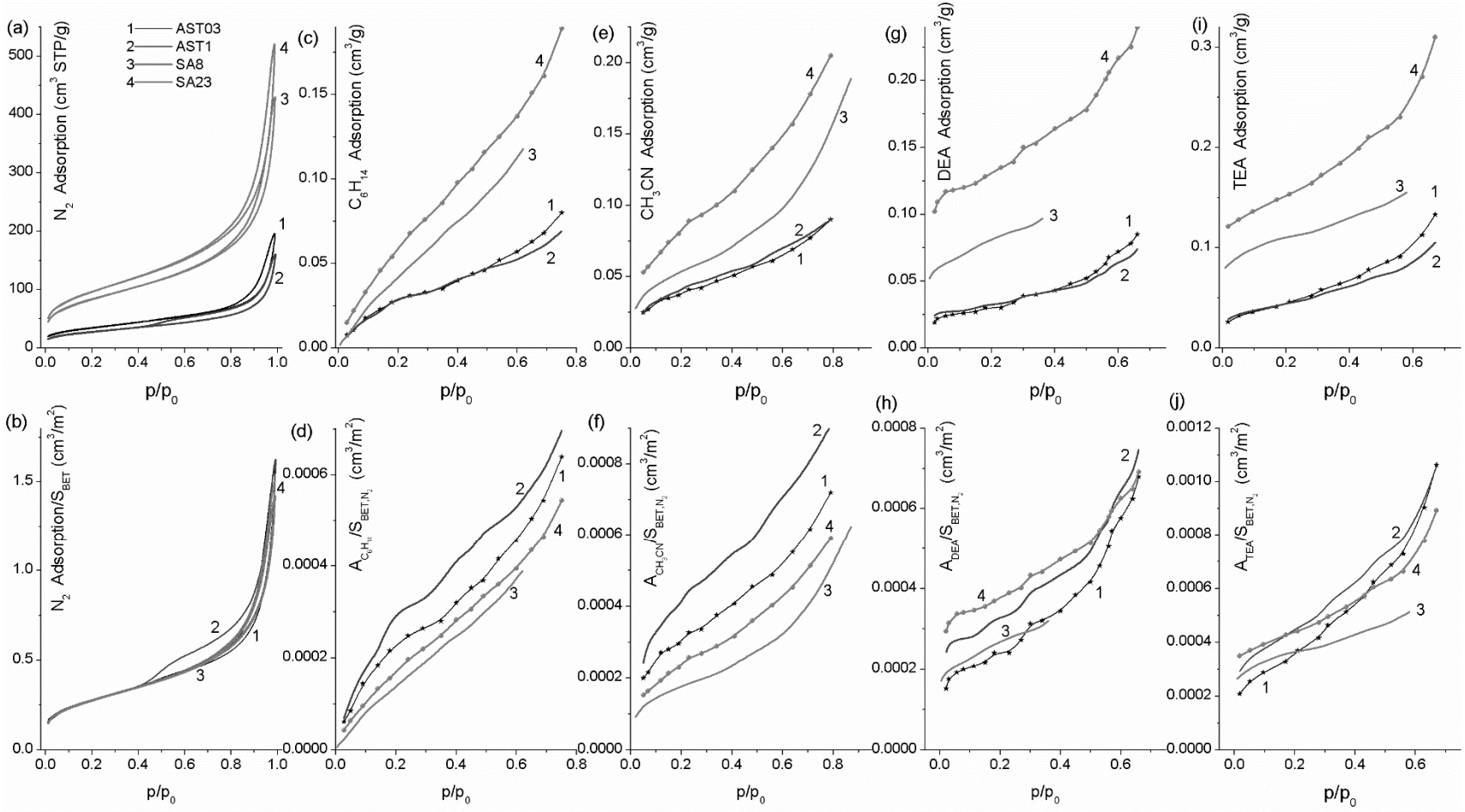

Fig. 7. Adsorption isotherms of (*a*, *b*) nitrogen, (*c*, *d*) hexane, (*e*, *f*) acetonitrile, (*g*, *h*) DEA, and (*i*, *j*) TEA (top – initial and bottom – normalized by S_{N_2}) onto FMO: (*1*) AST03, (*2*) AST1, (*3*) SA8, and (*4*) SA23 degassed at 200 °C

Greater differences in the probe adsorption on the same FMO are observed for more complex and/or polar adsorbates (DEA, TEA, CH_3CN, H_2O) than nitrogen (Figs. 4–8). These effects are caused by stronger bonding of stronger electron–donor and polar adsorbates to Brønsted (bridging hydroxyls) and Lewis (incompletely O–coordinated Al or Ti atoms) acid sites and other centers (*e.g.*, terminal hydroxyls) of complex FMO. However, there is a certain tendency toward a decrease in the adsorption of any adsorbates with decreasing SSA value, despite the difference in the polarity, electron–donor properties and molecular size of adsorbates. The strong influence of the SSA value on the adsorption of any adsorbates onto FMO is explained by the fact that a significant contribution to the adsorbed amounts is due to the first monolayer of adsorbates and insignificant capillary condensation of them in broad but short voids in supra–NPNP structures. Additional effects are due the difference in the nature and content of active surface sites (terminal (≡MOH) and bridging (≡M'O(H)M"≡) hydroxyls and others) at FMO surfaces responsible for the formation of strong adsorption complexes with electron–donor and proton–donor molecules. Note that long open hysteresis loops in the water, benzene, and hexane adsorption–desorption isotherms for pretreated A–300/AST1 blend (Fig. 8) are due to certain changes in the textural characteristics of the powder, *e.g.*, loosening of compacted supra–NPNP structures upon the interaction with the liquids causing swelling effects for supra–NPNP structures. Therefore, the desorption of molecules penetrated into narrow voids demonstrates certain delay resulting in the open hysteresis loops. In the case of water bound to initial AST1 or pretreated A–300/AST1 blend, the hysteresis loop could be also caused by dissociative adsorption of water molecules onto strained bonds at a surface of preheated degassed samples.

The preheating temperature of FMO plays an important role on the subsequent adsorption. However, morphological changes in fumed alumina (partially crystalline) are much smaller on heating than that of nanosilica [35, 36]. This effect is due to the difference in the types of hydroxyls (only terminal for silica and terminal and bridging for alumina and titania) and the O–coordinating numbers of Si (only fourfold O–coordinated) and Al (from fourfold to sixfold) or Ti (fivefold and sixfold O–coordinated) atoms [35, 36].

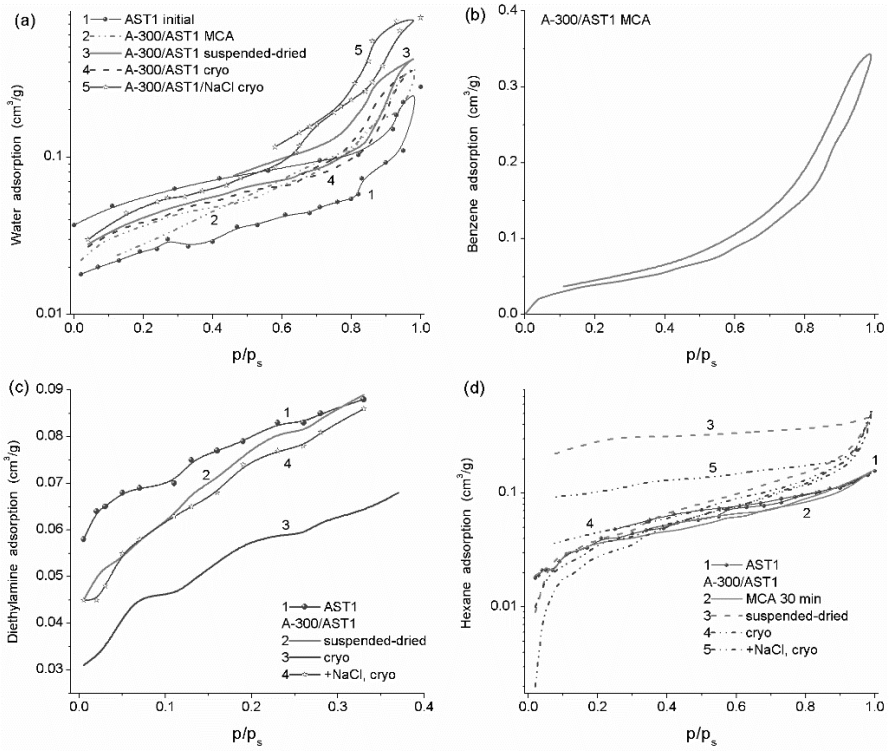

Fig. 8. Adsorption isotherms of (*a*) water, (*b*) benzene, (*c*) diethylamine, and (*d*) *n*–hexane onto initial and pretreated FMO individual AST1 and A–300/AST1 (1:1 w/w) blend

Therefore, associative desorption of water from silica leads to stronger changes in the lattice structure than for other studied oxides. Additionally, crystalline structure of alumina is much more rigid than that of amorphous silica that affect the morphological and textural changes of these FMO upon any strong pretreatment such as strong heating and cryogelation [36, 91].

Alumina (S_{N_2} = 133 m^2/g) preheated at 600 or 900 °C and cooled to room temperature (without contact to air) adsorbs greater amounts of acetonitrile and especially TEA than alumina degassed at 200 °C (Fig. 6 *b*). This result as well as large S_X/S_{N_2} value (Table 1) can be caused by enhancement of donor–acceptor interactions between the N atoms of adsorbed molecules and surface Lewis acid sites (effectively formed at a surface of strongly dehydrated alumina at high temperatures) and certain diminution of the size of primary particles (that results in increased SSA) on the strong heating due to associative (from hydroxyls) removal of water. Additionally, calcination at 900 °C can increase the crystallinity degree of alumina that can also influence the adsorption of electron–donor compounds. Notice that the first portion of adsorbates (especially water) can dissociatively adsorb onto strained bonds appearing at the oxide surface degassed at high temperatures [35, 36, 91].

The degree of NPNP aggregation (determining V_p value), which depends on treatment conditions, plays a certain role in the adsorption and changes in the S_X/S_{N_2} values. For example, for two samples of alumina, the ratio S_X/S_{N_2} is greater for a sample with a larger V_p value (Table 1) because the adsorption is greater for FMO with more aggregated smaller nanoparticles causing greater SSA (due to diminution of NPNP sizes). Additionally, variations in the orientation of adsorbed molecules at a surface affect the surface area (σ) occupied by each molecule and, therefore, the S_X/S_{N_2} ratio changes [35, 36, 74].

A minimal adsorption onto FMO preheated at 200 °C is observed for water (Figs. 4–8), despite the fact that it can form strong hydrogen bonds with surface hydroxyls (Tables 4–6, Fig. 9). The low adsorption of water is due to several reasons. First, saturated water vapor has low pressure (17.5 mm Hg at 20 °C). Second, water adsorption results in clustered structures rather than monolayered ones, *e.g.*, the surface is incompletely covered by water even at C_w = 15–20 wt. % corresponding to several statistical monolayers [35, 36]. Third, nanopores (nanovoids) give a small contribution to the pore volume, as well as narrow mesopores (Fig. 2). Among the adsorbates studied only water adsorbs in the form of clusters. Even during single molecule adsorption, it tends to form two hydrogen bonds with neighboring surface hydroxyls (Table 4). Therefore, nanopores and narrow mesopores are more appropriate for effective clustered or nanodomain adsorption of water than broad mesopores and macropores. In the latter, the formation of 3D structures totally filling broad meso/macrovoids needs great amounts of adsorbed water [35]. However, the adsorption of great amounts of water in broad pores at $p/p_0 < 0.99$ is thermodynamically unfavorable as well as for other studied adsorbates at ~ 20 °C. All the factors mentioned can play a certain role on the organics adsorption onto FMO surfaces. However, thermodynamic conditions upon their adsorption differ from that of water. This leads to greater adsorption of some organics onto complex FMO in comparison to water (Figs. 4–8) at the same temperature (~ 20 °C).

Nonpolar hexane and weakly polar acetonitrile adsorb better than water but worse than polar DEA and TEA. This is due to strong hydrogen bonding of the amines to the surface hydroxyls (B–acid sites) and L–acid sites. The adsorption of TEA is typically greater or close to that of nitrogen (at the same p/p_0 values), despite a large difference in the adsorption temperatures (20 °C and −195.8 °C, respectively). Temperature determines the average kinetic energy of molecules, and elevating temperature leads to diminution of the physical adsorption especially in broad voids in supra–NPNP structures where the steric effects are absent but the interactions with distant NPNP surfaces are very weak.

In contrast to dispersion interactions of hexane and nitrogen with FMO, specific interactions of acetonitrile and amines with surface active sites can cause an overestimation of the S_X value in comparison with the S_{N_2} or S_{hex} values (Table 1). This is due to several effects caused by features of orientation and packing of molecules in the first adsorbed layer, as well as

Table 4. Interaction energy of DEA, TEA, and water with SA and silica clusters (ωB97X–D/cc–pVDZ) estimated using FMCC/BSSE and simple FM

Complex type	**Cluster model**	**E_t (Ha)**	**ΔE (kcal/mol)**	**ΔE per 1 molecule (kcal/mol)**	**Note**
1	2	*3*	4	5	6
SA···2DEA	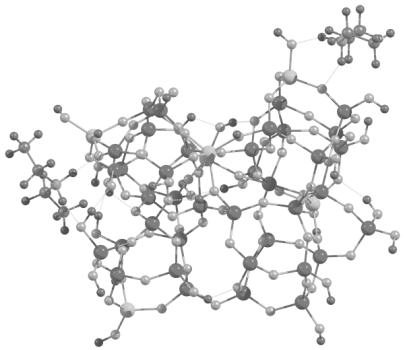	–20429.5482709	–66.6	–33.3	FM
		–20429.518882572927	–273.1	–136.5	FMCC/BSSE 2DEAH···SA q = 0.558, 0.408, –0.965
SA···2DEA		–20429.114585360207	–258.4	–129.2	FMCC/BSSE $2DEAH^{+}\cdots SA^{-2}$ q = 0.764, 0.654, –1.418
SA···2TEA	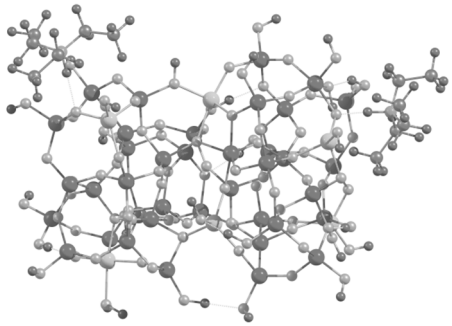	–20586.7590723	–107.1	–45.4	FM
		–20586.708701821837	–280.5	–140.2	FMCC/BSSE $2TEAH^{+}\cdots SA^{-}$ q= 0.535, 0.442, –0.977
SA···$2H_2O$	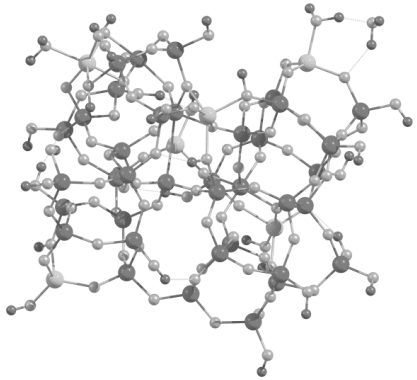	–20154.8693088	–65.2	–32.6	FM
		–20154.842166758495	–285.3	–142.6	FMCC/BSSE q= 0.192, 0.306, –0.498

1	2	3	4	5	6
SiO_2···2DEA	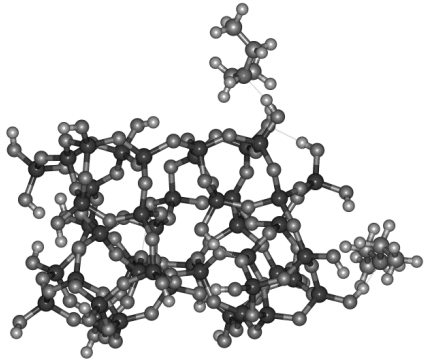	–20708.0542610	–46.3	–23.2	FM
		–20707.979222095877	–15.5	–7.7	FMCC/BSSE H bonds with siloxane bridges q=–0.064, –0.067, 0.131
		–20707.966738519899	–40.3	–20.1	H bonds with silanol hydroxyls *q*= 0.087, 0.054, –0.140
SiO_2···2TEA	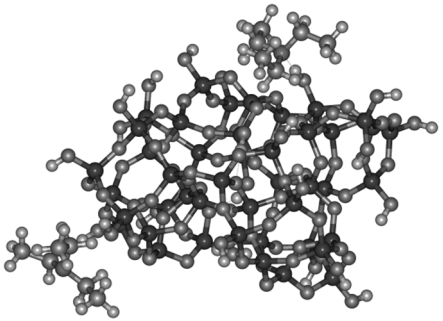	–20865.2451507	–58.1	–29.1	FM
		–20865.175610715305	–31.4	–15.7	FMCC/BSSE *q*= 0.049, –0.066, 0.017
SiO_2···2H_2O	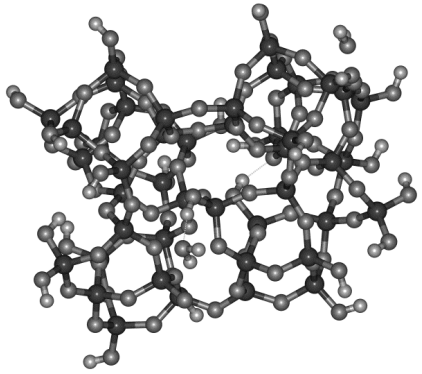				FM
		–20433.3542283	–31.7	–15.9	without solvation
		–20433.5331716	–46.1	–23.1	with solvation
		–20433.298524647918	–21.0	–10.5	FMCC/BSSE *q*= 0.078, 0.102, –0.180

Note. *q* is the charge of two bound molecules and cluster (fragments), respectively

conformational changes of the adsorbed molecules. Orientation of adsorbed molecules interacting with surface hydroxyls, especially bridging ones, can correspond to their non–maximal projection onto the surface. Therefore, the effective σ value can be smaller than the value estimated from the molecular geometry of free adsorbates resulting in the SSA overestimation. This overestimation is maximal for acetonitrile. Its adsorption complexes mainly correspond to non–lengthwise orientation of the molecules that causes a significant diminution of the effective σ value [36, 74]. However, the σ value for acetonitrile used for estimation of S_{ac} (Table 1) corresponds to the average projection area of a molecule to a surface.

The S_X overestimation for TEA is greater than that for DEA for samples at $S_{N_2} \leq 125$ m^2/g, significant crystallinity and surface roughness [74]. However, for SA8 and SA23 with large S_{N_2} values and predominant phases with amorphous silica and alumina, this effect is greater for DEA. These results can be caused by different changes in the packing of adsorbed molecules of DEA and TEA in the first monolayer at the surface of smaller nanoparticles more strongly aggregated in supra–NPNP structures because the steric factor is lower for smaller DEA molecules than for TEA and it is smaller for FMO with larger NPNP less aggregated. Consequently, this factor should be greater for FMO samples with larger S_{BET} value because they are characterized by enhanced aggregation of nanoparticles [35, 36]. For hexane, the S_{hex} overestimation is observed for alumina degassed at 200 and 900 °C [74].

Theoretical modeling of adsorption. Some aspects of interactions between different FMO (*e.g.*, SA and silica) and various probe adsorbates could be elucidated using quantum chemical calculations (Tables 4–6, Fig. 9). An increase in size of an adsorbent cluster results in an increase in interaction energy and increased intermolecular bonds between adsorbed molecules and clusters (Tables 4–6). This result is due to enhanced polarization of bound molecules and charge transfer that are greater for larger clusters more strongly affecting adsorbed molecules (Table 4).

The use of the fragment method with counterpoise (and BSSE) corrections gives overestimated values of the interaction energy due to non–weak interactions between adsorbate and adsorbent with transfer of significant charge (Table 4, *q*) in contrast to the results of the calculations with the Kitaura–Morokuma method using a small oxide cluster (Table 6). However, even in the case of a small cluster, the electrostatic component ΔE_{el} of the total interaction energy is large (predominant) for polar molecules in contrast to nonpolar ones (Table 6).

Table 5. Interaction energy of DEA and TEA with SA and silica clusters (see Table 4) with consideration of the solvation effects in DEA and TEA, respectively (SMD/ωB97X–D/cc–pVDZ)

Interaction	E_t (Ha)	Δ*E* (kcal/mol)	Δ*E* per a molecule (kcal/mol)
SA···2DEA	–20430.6057799432	–281.09	–140.5
SA···2TEA	–20587.7942521895	–283.98	–142.0
SiO_2···2DEA	–20709.1313956562	–19.06	–9.5
SiO_2···2TEA	–20866.3578504207	–36.87	–18.4

Table 6. Interaction energy between Brønsted acid site =(HO)SiO(H)Al(OH)= (as a simple model of SA) and an adsorbate molecule calculated using the Kitaura–Morokuma method (6–31G(d,p) basis set)

Adsorbate	ΔE_{HF} (kcal/mol)	ΔE_{BSSE} (kcal/mol)	ΔE_{el} (kcal/mol)
H_2O	–16.6	–13.5	–26.0
NH_3	–18.0	–15.6	–28.9
CH_3CN	–9.7	–8.6	–12.5
N_2	–1.9	–1.2	–2.2
C_6H_{14}	–1.1	–0.4	–0.4

Note. ΔE_{HF} is the changes in the total energy on the bonding, ΔE_{BSSE} is the ΔE value with consideration for the basis set superposition error (BSSE) and $-\Delta E_{HF} > -\Delta E_{BSSE}$, and ΔE_{el} is the electrostatic component of ΔE_{HF}

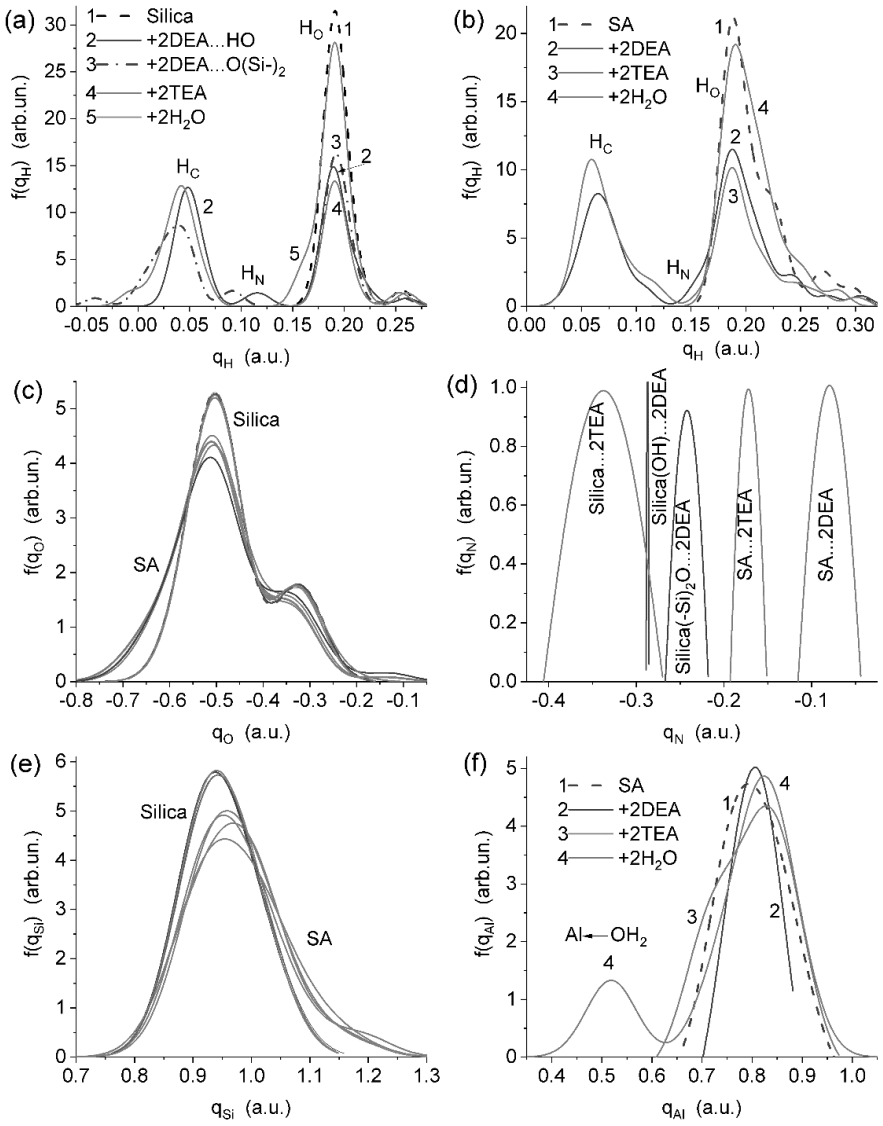

Fig. 9. Atomic charge distribution functions for H atoms in adsorption complexes with (*a*) silica and (*b*) alumina/silica; and atoms of (*c*) O, (*d*) N, (*e*) Si, and (*f*) Al in adsorption complexes of DEA, TEA, and water molecules (two molecules in each system, Table 4)

The SMD/EDA calculations with consideration of the solvation effects using large clusters (Table 5) give results similar to that of FMCC/BSSE (Table 4). The interaction energy overestimation could be also explained by the formation of several intermolecular bonds between a molecule and a cluster (see structures in Table 4). As a whole, the used approaches show decreased interaction energy for TEA > DEA (or NH_3 in Table 6) > H_2O that also corresponds to the charge transfer values (Table 4, *q*) and the interactions are much stronger for SA clusters with any adsorbates than that for silica ones (Table 4). These results correlate to the experimental adsorption measurements, *e.g.*, showing more strongly enhanced SSA values estimated for adsorbates forming strong intermolecular bonds with complex FMO or alumina adsorbents in comparison to fumed silica (Tables 1–3) that also is in agreement with higher adsorption activity of various surface sites at a surface of complex FMO and alumina in comparison to silica (Fig. 3).

Note that the orientation of bound molecules with respect to a cluster surface varies depending on the types of adsorbates and adsorbents and the structure of adsorption sites (Table 4). Obtained results explain the effects of changes in the SSA estimated using different adsorbates not only due to the orientation of the molecules but also certain

changes in their conformation especially for strong complexes between polar molecules and active surface sites affected by charge transfer.

The charge distribution functions (Fig. 9) show that the interactions between bound molecules and oxide clusters strongly affect mainly atoms H (in B–sites), electron–donor N (in bound DEA and TEA) or O (in adsorbates (water) and surface hydroxyls), and Al (in L–sites with bound adsorbate) forming the intermolecular bonds. The CDF are more stable for O (Fig. 9 *c*) and Si (Fig. 9 *e*) for silica than those for the SA clusters with bound adsorbates because of stronger bonding for the latter.

CONCLUSION

Performed investigations of the adsorption of polar, weakly polar and nonpolar adsorbates (X) onto individual and complex FMO show that the ratio S_X/S_{N_2} depends on the textural, morphological, and structural characteristics of adsorbents, the nature and amounts of active surface sites, conditions of FMO degassing, the polarity of adsorbates and their ability to form strong hydrogen (with surface Brønsted acid sites) or donor–acceptor (with Lewis acid sites) bonds with the FMO surface. A larger overestimation of the specific surface area S_X was found for complex FMO at S_{N_2} = 100–133 m^2/g and high roughness of nanoparticles than that at smaller (with weaker aggregated nanoparticles) or larger S_{N_2} of FMO with lower crystallinity and with lower Brønsted acidity but stronger aggregated. Additionally, changes in the S_X/S_{N_2} ratio can correlate to changes in the oxide hydrophilicity, *i.e.*, strength and acidity of surface sites. The amounts of water bound to FMO nanoparticles in the aqueous suspensions are much larger than the pore volume V_{p,N_2} of the initial powders or dried solid residua of the suspension of the same materials. This is due to different rearrangements of supra–NPNP structures in the strongly wetted powders and aqueous suspensions of FMO. Therefore, the rearrangement of the supra–NPNP structures under action of adsorbates or/and solvents can affect the adsorption capacity and energetic characteristics as well as interactions of nanoparticles with their surroundings in complex liquid and polymer media. The results obtained show that not only the specific surface area, pore volume, pore size distributions, and particle sizes but also surface composition of the surface phases, surface roughness, and rearrangement of nanoparticles affect the adsorption energy of different adsorbates, the adsorbed layer structure, and the behavior of the interfacial layer at different temperatures. This influence is maximal for adsorbates forming the strong hydrogen and donor–acceptor bonds with most active surface sites. The study shows that the use of the S_{BET} values based on the nitrogen adsorption isotherms during consideration of adsorption of various adsorbates could generate some systematic errors (*e.g.*, in adsorption per SSA unit) since the surface accessibility for complex adsorbates depends on several factors related to the adsorbent texture and adsorbate characteristics. Additionally, adsorbents such as 'soft' FMO can strongly change the organization of supra-NPNP structures under action of any adsorbate or any treatment (even gentle one). These changes depend on the adsorbate characteristics; therefore, under the comparison of the adsorption of different probes, these effects and possible differences in adsorbates impact should be taken into account. The effects described here could be of importance for the optimization of the characteristics of the FMO materials for a range of applications including adsorbents, fillers, additives, *etc*. In the future, it could be of interest to provide a complex study of adsorption of various adsorbates onto various carbons, porous oxides and polymers well characterized using a set of experimental and theoretical methods.

ACKNOWLEDGEMENTS

V.M.G. is grateful to the National Research Foundation of Ukraine (Support of advanced and young scientists, grant 2020.02/0057) for financial support of this study, and to Gaussian, Inc. for the Gaussian 16, Revision C.02 program suit.

Адсорбція різних сполук на нанооксидах, вихідних та по–різному тренованих

В.М. Гунько, О.К. Матковський

Інститут хімії поверхні ім. О.О. Чуйка Національної академії наук України
вул. Генерала Наумова, 17, Київ, 03164, Україна, vlad_gunko@ukr.net

Особливості міжфазних явищ адсорбат/адсорбент залежать від кількох факторів: морфології частинок, текстури та структури адсорбентів, молекулярної маси та форми, полярності адсорбатів; а також від передісторії адсорбентів, наприклад, «м'яких» порошків нанооксидів, попередньо оброблених у різних умовах. Усі ці фактори можуть впливати на ефективність практичного застосування не лише адсорбентів, а й полімерних наповнювачів, носіїв, каталізаторів тощо. Взаємодія неполярних таких адсорбатів, як азот, гексан та бензол, слабкополярного ацетонітрилу, полярних ді– та триетиламінів, води з індивідуальними (кремнезем, оксид алюмінію), бінарними (діоксид кремнію/оксид алюмінію (SA)) і потрійними (оксид алюмінію/оксид кремнію/оксид титану, AST) нанооксидами досліджували за допомогою експериментальних і теоретичних методів для з'ясування впливу морфологічних і текстурних характеристик і складу поверхні матеріалів на явища адсорбції. Співвідношення питомої площі поверхні S_X /S_{N_2} (X – адсорбат) змінюється від 0.7 для гексану, адсорбованого на аморфному SA8 з 8 мас. % Al_2O_3 (дегазованого при 200 °C) до 1.9 для ацетонітрилу, адсорбованого на чистому пірогенному оксиді алюмінію (обробленому при 900 °C). Ці зміни є відносно великими через варіації орієнтації, латеральних взаємодій та адсорбційного стиснення органічних молекул, які взаємодіють з поверхнями, що характеризуються певним набором і кількістю різноманітних активних центрів, а також через зміни доступності поверхні пор для молекул різних розмірів. Більші значення S_X /S_{N_2} > 1 спостерігаються для складних нанооксидів з більшими первинними наночастинками, більшою шорсткістю поверхні, гідрофільністю та кислотністю (центри Бренстеда і Льюїса) поверхні. Як полярні, так і неполярні адсорбати можуть змінювати морфологію і текстуру агрегатів наночастинок оксидів, наприклад, призводити до набухання структур (ущільнених під час різних попередніх обробок) при адсорбції рідин. Вивчені ефекти треба враховувати при практичному застосуванню адсорбентів, особливо таких, як «м'які» нанооксиди.

Ключові слова: *наночастинки оксидів, складні нанооксиди, текстурні характеристики, неполярні адсорбати, полярні адсорбати, явища на межах поділу*

REFERENCES

1. *Ullmann's Encyclopedia of Industrial Chemistry*. (Weinheim: Wiley–VCH, 2008).
2. Hastie J.W. (editor). Materials Chemistry at High Temperatures. V. 1, Characterization. V. 2, Processing and Performance. (NJ Clifton: Humana Press, 1990).
3. Büchel K.H., Moretto H.–H., Woditsch P. *Industrial inorganic chemistry*. (Weinheim: Wiley–VCH Verlag GmbH, 2000).
4. *Basic characteristics of Aerosil fumed silica* (4th ed.). Tech. Bull. Fine Particles 11. (Hanau: Evonik Industries, 2014).
5. *Cabot Corporation*. http://www.cabotcorp.com/solutions/products–plus/fumed–metal–oxides/. CAB–O–SIL® fumed silicas for pharmaceutical and nutraceutical applications.
6. *DuPont*. http://www.dupont.com/
7. *Evonik Ind*. http://corporate.evonik.com/en/Pages/default.aspx http://www.aerosil.com/product/aerosil/en/services/downloads/Pages/test–methods.aspx
8. *Wacker Chemie Ag*. https://www.wacker.com/cms/en/products/brands_2/hdk/hdk.jsp
9. *Hongwu International Group Ltd*. http://www.hwnanomaterial.com/The–Difference–Between–Hydrophilic–Silica–and–Hydrophobic–Silica–Nanoparticles_p255.html
10. Yang R.T. Adsorbents: Fundamentals and Applications. (New York: Wiley, 2003).
11. Theodore L., Kunz R. G. *Nanotechnology: Environmental Implications and Solutions*. (Hoboken, N.J.: John Wiley & Sons, 2005).
12. Wypych G. *Handbook of Fillers*. (Toronto: ChemTec Publishing, 1999).
13. Rothon R.N., Roger N. *Particulate fillers for polymers*. (Shrewsbury: Rapra, 2001).

14. Somasundaran P. (editor). *Encyclopedia of Surface and Colloid Science.* Third Edition. (Boca Raton: CRC Press, 2015).
15. Blitz J.P., Gun'ko V.M. (editors). *Surface Chemistry in Biomedical and Environmental Science*. NATO Science Series II: Mathematics, Physics and Chemistry. V. 228. (Dordrecht: Springer, 2006).
16. Iler R.K. The Chemistry of Silica: Solubility, Polymerization, Colloid and Surface Properties and Biochemistry of Silica. (Chichester: Wiley, 1979).
17. Bergna H.E., Roberts W.O. (editors). *Colloidal Silica: Fundamentals and Applications*. (Boca Raton: CRC Press, 2006).
18. Theodore L. Nanotechnology: Basic Calculations for Engineers and Scientists. (Hoboken, N.J.: John Wiley & Sons, 2006).
19. Hashim A.A. (editor). *Smart Nanoparticles Technology*. (Rijeka, Croatia: InTech, 2012).
20. Biricik H., Sarier N. Comparative study of the characteristics of nano silica–, silica fume– and fly ash – incorporated cement mortars. *Mater. Res.* 2014. **17**(3): 570.
21. Slejko F.L. Adsorption Technology: A Step–by–Step Approach to Process Evaluation and Application. (New York: Marcel Dekker Inc., 1985).
22. Lu K. Nanoparticulate Materials. Synthesis, Characterization, and Processing. (Hoboken, New Jersey: John Wiley & Sons, Inc., 2013).
23. Birdi K.S. (editor). *Handbook of Surface and Colloid Chemistry*. Third edition. (Boca Raton: CRC Press, 2009).
24. Legrand A.P. (editor). *The Surface Properties of Silicas*. (New York: Wiley, 1998).
25. Vansant E.F., Van Der Voort P., Vrancken K.C. *Characterization and Chemical Modification of the Silica Surface*. (Amsterdam: Elsevier, 1995).
26. Dabrowski A., Tertykh V.A. (editors). Adsorption on New and Modified Inorganic Sorbents; Studies in Surface Science and Catalysis. V. 99. (Amsterdam: Elsevier, 1996).
27. Auner N., Weis J. (editors). *Oganosilicon Chemistry* VI. (Weinheim: Wiley–VCH Verlag GmbH, 2005).
28. Piemonte V., De Falco M., Basile A. (editors). *Sustainable Development in Chemical Engineering – Innovative Technologies. First Edition*. (Chichester, UK: John Wiley & Sons, 2013).
29. Buesser B., Pratsinis S.E. Design of aerosol particle coating: Thickness, texture and efficiency. *Chem. Eng. Sci*. 2010. **65**(20): 5471.
30. Pietsch W. *Agglomeration in Industry*. (Weinheim: Wiley–VCH Verlag GmbH, 2005).
31. Kulkarni P., Baron P.A., Willeke K. (editors). *Aerosol Measurement: Principles, Techniques, and Applications*. Third Edition. (New York: John Wiley & Sons, 2011).
32. Oberdisse J. Aggregation of colloidal nanoparticles in polymer matrices. *Soft Matter.* 2006. **2**(1): 29.
33. Brunelli A., Pojana G., Callegaro S., Marcomini A. Agglomeration and sedimentation of titanium dioxide nanoparticles (n–TiO_2) in synthetic and real waters. *J. Nanopart. Res*. 2013. **15**:1684.
34. Tapia O., Bertrán J. (editors). *Solvent Effects and Chemical Reactivity*. (New York: Kluwer Academic Publishers, 2000).
35. Gun'ko V.M., Turov V.V. Nuclear Magnetic Resonance Studies of Interfacial Phenomena. (Boca Raton: CRC Press, 2013).
36. Gun'ko V.M., Turov V.V., Zarko V.I., Goncharuk O.V., Pahklov E.M., Skubiszewska–Zięba J., Blitz J.P. Interfacial phenomena at a surface of individual and complex fumed nanooxides. *Adv. Colloid Interface Sci.* 2016. **235**: 108.
37. Henderson M.A. Interaction of water with solid surfaces: fundamental aspects revisited. *Surf. Sci. Report*. 2002. **46**(1–8): 1.
38. Wypych G. (editor). *Handbook of Solvents*. (Toronto: ChemTec Publishing, 2001).
39. Kammerhofer J. *Capillary Wetting of Heterogeneous Powders.* 1st edn. (Göttingen: Cuvillier Verlag, 2019).
40. Mittal V. (editor). *Surface Modification of Nanoparticle and Natural Fiber Fillers*. First Edition. (Weinheim: Wiley–VCH, 2015).
41. Kim C.–S., Randow C., Sano T. (editors). *Hybrid and Hierarchical Composite Materials*. (Switzerland: Springer, 2015).
42. Kickelbick G. (editor). Hybrid Materials. Synthesis, Characterization, and Applications. (Weinheim: Wiley–VCH, 2007).
43. Ajayan P.M., Schadler L.S., Braun P.V. *Nanocomposite Science and Technology*. (Weinheim: Wiley–VCH, 2003).
44. Balazs C., Emrick T., Russell T.P. Nanoparticle polymer composites: Where two small worlds meet. *Science.* 2006. **314**(5802): 1107.
45. Zou H., Wu S., Shen J. Polymer/silica nanocomposites: preparation, characterization, properties, and applications. *Chem. Rev*. 2008. **108**(9): 3893.
46. Schmidt G., Malwitz M.M. Properties of polymer – nanoparticle composites. *Curr. Opin. Colloid Interface Sci.* 2003. **8**(1): 103.

47. Kumar M.S.S., Raju N.M.S., Sampath P.S., Jayakumari L.S. Effects of nanomaterials on polymer composites – an expatiate view. *Rev. Adv. Mater. Sci.* 2014. **38**(1): 40.
48. Díaz A., Casas M.T., Puiggalí J., Dispersion of functionalized silica micro– and nanoparticles into poly(nonamethylene azelate) by ultrasonic micro–molding. *Appl. Sci*. 2015. **5**(4): 1252.
49. Bagwe R.P., Hilliard L.R., Tan W. Surface modification of silica nanoparticles to reduce aggregation and nonspecific binding. *Langmuir*. 2006. **22**(9): 4357.
50. Nicolais L., Borzacchiello A., Lee S.M. (editors). *Wiley Encyclopedia of Composite Materials*, 5–Volume set, 2nd ed. (Hoboken, NJ: Wiley, 2012).
51. Gregg S.J., Sing K.S.W. *Adsorption, Surface Area and Porosity*. 2nd ed. (London: Academic Press, 1982).
52. Adamson A.W., Gast A.P. *Physical Chemistry of Surface*. Sixth edn. (New York: Wiley, 1997).
53. Lowell S., Shields J., Thomas M.A., Thommes M. Characterization of Porous Solids and Powders: Surface Area, Porosity and Density. (Dordrecht: Springer, 2004).
54. Rouquerol J., Rouquerol F., Sing K.S.W., Llewellyn P., Maurin G. *Adsorption by Powders and Porous Solids: Principles, Methodology and Applications.* (New York: Academic Press, 2014).
55. Thommes M., Kaneko K., Neimark A.V., Olivier J.P., Rodriguez–Reinoso F., Rouquerol J., Sing K.S.W. Physisorption of gases, with special reference to the evaluation of surface area and pore size distribution (IUPAC Technical Report). *Pure Appl. Chem*. 2015. **87**(9–10): 1051.
56. Sing K.S.W., Everett D.H., Haul R.A.W, Moscou L., Pieroti R.A., Rouquerol J., Siemieniewska T. Reporting physisorption data for gas/solid systems with special reference to the determination of surface area and porosity (Recommendations 1984). *Pure Appl. Chem*. 1985. **57**(4): 603.
57. LeVan M.D. (editor). *Fundamentals of Adsorption*. (Boston: Kluwer Academic Publishers, 1996).
58. Nguyen C., Do D.D. A new method for the characterization of porous materials. *Langmuir.* 1999. **15**(10): 3608.
59. Al–Abadleh H.A., Grassian V.H. Oxide surfaces as environmental interfaces. *Surf. Sci. Report*. 2003. **52**(3–4): 63.
60. Henderson M.A. The interaction of water with solid surfaces: fundamental aspects revisited. *Surf. Sci. Rep*. 2002. **46**(1–8): 1.
61. Akhter F., Rao A.A., Abbasi M.N., Wahocho S.A., Mallah M.A.,·Anees–ur–Rehman H., Chandio Z.A. A comprehensive review of synthesis, applications and future prospects for silica nanoparticles (SNPs). *Silicon.* 2022. **14**: 8295.
62. Canesi L., Ciacci C., Vallotto D., Gallo G., Marcomini A., Pojana G. In vitro effects of suspensions of selected nanoparticles (C60 fullerene, TiO_2, SiO_2) on Mytilus hemocytes. *Aquat. Toxicol*. 2010. **96**(2):151.
63. D'Agata A., Salvatore F., Dallas L.J., Fisher A.S., Maisano M., Readman J.W., Jha A.N. Enhanced toxicity of 'bulk' titanium dioxide compared to 'fresh' and 'aged' nano–TiO_2 in marine mussels (Mytilus galloprovincialis). *Nanotoxicology.* 2014. **8**(5): 549.
64. Njuguna J., Pielichowski K., Zhu H. (editors). Health and Environmental Safety of Nanomaterials. Polymer Nancomposites and Other Materials Containing Nanoparticles. (Cambridge: Woodhead Publishing, 2021).
65. Srikanth K., Mahajan A., Pereira E., Duarte A.C., Rao J.V. Aluminium oxide nanoparticles induced morphological changes, cytotoxicity and oxidative stress in Chinook salmon (CHSE–214) cells. *J. Appl. Toxicol*. 2015. **35**(10): 1133.
66. Younes M., Aggett P., Aguilar F., Crebelli R., Dusemund B., Filipic M., Frutos M.J., Galtier P., Gott D., Gundert–Remy U., Kuhnle G.G., Leblanc J.–C., Lillegaard I.T., Moldeus P., Mortensen A., Oskarsson A., Stankovic I., Waalkens–Berendsen I., Woutersen R.A., Wright M., Boon P., Chrysafidis D., Gurtler R., Mosesso P., Parent–Massin D., Tobback P., Kovalkovicova N., Rincon A.M., Tard A., Lambre C. Re–evaluation of silicon dioxide (E 551) as a food additive. *EFSA Journal*. 2018. **16**(1): 5088.
67. Shpak A.P., Gorbik P.P. (editors). *Nanomaterials and Supramolecular Structures*. (Dordrecht: Springer, 2010).
68. Chuiko A.A. (editor). *Chemistry of silica surface.* (Kyiv: UkrINTEI, 2001). [in Russian].
69. Chuiko A.A. (editor). *Medical chemistry and clinical application of silica*. (Kyiv: Naukova Dumka, 2003). [in Russian].
70. Gun'ko V.M. Interfacial phenomena: effects of confined space and structure of adsorbents on the behavior of polar and nonpolar adsorbates at low temperatures. *Current Physical Chemistry*. 2015. **5**: 137.
71. Gun'ko V.M. Various methods to describe the morphological and textural characteristics of various materials. *Him. Fiz. Tehnol. Poverhni.* 2018. **9**: 317.
72. Gun'ko V.M., Voronin E.F., Nosach L.V., Turov V.V., Wang Z., Vasilenko A.P., Leboda R., Skubiszewska–Zięba J., Janusz W., Mikhalovsky S.V. Structural, textural and adsorption characteristics of nanosilica mechanochemically activated in different media. *J. Colloid Interface Sci.* 2011. **355**: 300.
73. Gun'ko V.M., Turov V.V., Pakhlov E.M., Krupska T.V., Charmas B. Effect of water content on the characteristics of hydro–compacted nanosilica. *Appl. Surf. Sci*. 2018. **459**: 171.
74. Gun'ko V.M., Yurchenko G.R., Turov V.V., Goncharuk E.V., Zarko V.I., Zabuga A.G., Matkovsky A.K., Leboda R., Skubiszewska–Zięba J., Janusz W., Phillips G.J., Mikhalovsky S.V. Adsorption of polar and nonpolar compounds onto complex nanooxides with silica, alumina, and titania. *J. Colloid Interface Sci*. 2010. **348**(2): 546.

75. Brunauer S., Emmett P.H., Teller E. Adsorption of gases in multimolecular layers. *J. Am. Chem. Soc.* 1938. **60**(2): 309.
76. Gun'ko V.M. Textural characteristics of composite adsorbents analyzed with density functional theory and self–consistent regularization procedure. *Him. Fiz. Tehnol. Poverhni.* 2020. **11**(2): 163.
77. Nguyen C., Do D.D. Effects of probing vapors and temperature on the characterization of micro–mesopore size distribution of carbonaceous materials. *Langmuir.* 2000. **16**: 7218.
78. Do D.D., Nguyen C., Do H.D. Characterization of micro–mesoporous carbon media. *Colloids Surf. A.* 2001. **187–188**: 51.
79. Provencher S.W. A constrained regularization method for inverting data represented by linear algebraic or integral equations. *Comput. Phys. Comm*. 1982. **27**(3): 213.
80. Frisch M.J., Trucks G.W., Schlegel H.B., Scuseria G.E., Robb M.A., Cheeseman J.R., Scalmani G., Barone V., Petersson G.A., Nakatsuji H., Li X., Caricato M., Marenich A.V., Bloino J., Janesko B.G., Gomperts R., Mennucci B., Hratchian H.P., Ortiz J.V., Izmaylov A.F., Sonnenberg J.L., Williams–Young D., Ding F., Lipparini F., Egidi F., Goings J., Peng B., Petrone A., Henderson T., Ranasinghe D., Zakrzewski V.G., Gao J., Rega N., Zheng G., Liang W., Hada M., Ehara M., Toyota K., Fukuda R., Hasegawa J., Ishida M., Nakajima T., Honda Y., Kitao O., Nakai H., Vreven T., Throssell K., Montgomery J.A. Jr., Peralta J.E., Ogliaro F., Bearpark M.J., Heyd J.J., Brothers E.N., Kudin K.N., Staroverov V.N., Keith T.A., Kobayashi R., Normand J., Raghavachari K., Rendell A.P., Burant J.C., Iyengar S.S., Tomasi J., Cossi M., Millam J.M., Klene M., Adamo C., Cammi R., Ochterski J.W., Martin R.L., Morokuma K., Farkas O., Foresman J.B., Fox D.J. *Gaussian 16, Revision C.02*, (Gaussian, Inc., Wallingford CT, 2019).
81. Barca G.M.J., Bertoni C., Carrington L., Datta D., De Silva N., Deustua J.E., Fedorov D.G., Gour J.R., Gunina A.O., Guidez E., Harville T., Irle S., Ivanic J., Kowalski K., Leang S.S., Li H., Li W., Lutz J.J., Magoulas I., Mato J., Mironov V., Nakata H., Pham B.Q., Piecuch P., Poole D., Pruitt S.R., Rendell A.P., Roskop L.B., Ruedenberg K. Recent developments in the general atomic and molecular electronic structure system. *J. Chem. Phys.* 2020. **152**(15): 154102.
82. Marenich A.V., Cramer C.J., Truhlar D.G. Universal solvation model based on solute electron density and on a continuum model of the solvent defined by the bulk dielectric constant and atomic surface tensions. *J. Phys. Chem. B.* 2009. **113**(18): 6378.
83. Engel E., Dreizler R.M. *Density Functional Theory: An Advanced Course*. (Dordrecht: Springer, 2013).
84. Helgaker T., Jorgensen P., Olsen J. *Molecular Electronic Structure Theory*. (John Wiley & Sons, 2014).
85. Martin R.M., Reining L., Ceperley D.M. *Interacting Electrons*. (Cambridge University Press, 2016).
86. Gun'ko V.M. Atomic charge distribution functions as a tool to analyze electronic structure of molecular and cluster systems. *Int. J. Quantum Chem*. 2021. **121**(14): e26665.
87. Pettersen E.F., Goddard T.D., Huang C.C., Meng E.C., Couch G.S., Croll T.I., Morris J.H., Ferrin T.E. UCSF Chimera X: Structure visualization for researchers, educators, and developers. *Protein Sci.* 2021. **30**(1): 70.
88. *Avogadro 2*. https://two.avogadro.cc/. Ver. 1.97. 2023
89. Zhurko G.A., Zhurko D.A. *Chemcraft* (version 1.8, build 640). http://www.chemcraftprog.com
90. *Jmol: an open–source Java viewer for chemical structures in 3D* (Ver. 16.1.11). http://www.jmol.org/
91. Gun'ko V.M., Turov V.V., Goncharuk O.V., Pakhlov E.M., Matkovsky O.K. Interfacial phenomena at a surface of individual and complex fumed nanooxides. *Surface*. 2019. **11(26)**: 3.

Received 03.05.2023, accepted 27.11.2023